AIAA JOURNAL
Vol. 37, No. 10, October 1999

High-Order-Accurate Methods for Complex Unsteady Subsonic Flows

Miguel R. Visbal* and Datta V. Gaitonde†
U.S. Air Force Research Laboratory, Wright–Patterson Air Force Base, Ohio 45433-7521

Several issues related to the application of very high-order schemes for the finite difference simulation of the full Navier–Stokes equations are investigated. The schemes utilize an implicit, approximately factored time-integration method coupled with spatial fourth- and sixth-order compact-difference formulations and a filtering strategy of up to tenth order. For this last aspect a consistent optimization approach is developed to treat points near the boundary resulting in minimal degradation of accuracy. The problems investigated exhibit many of the challenging features of practical flows and include several with complications introduced by curvilinear meshes, viscous effects, unsteadiness, and three-dimensionality. The high-order method is observed to be very robust for every problem considered. The algorithm is demonstrated to be highly accurate compared to both second-order and upwind-biased methods. For several cases, particularly very-low-Mach-number flows, filtering is determined to be a superior alternative to scalar damping.

I. Introduction

DESPITE rapid improvements in computational technology, the numerical simulation of a wide range of practical turbulence,[1] aeroacoustic,[2] and electromagnetic[3] phenomena remains intractable. One example is the direct simulation of high Reynolds-number wall-bounded flows. A common thrust in each of the preceding disciplines has been directed at developing more accurate methods that maintain the error below a prescribed limit even for a relatively small number of points per wave. Some approaches include spectral (see Refs. 4 and 5 for example), optimized lower-order,[2] and higher-order[6,7] techniques.

The specific objective of this work is to develop, implement, and analyze higher-order—defined here to be higher than third—accurate schemes for the compressible Navier–Stokes equations (Sec. II). The focus is particularly on complicated subsonic vortical flow problems with nontrivial geometries and/or boundary conditions. A primary component of this study is the examination of the higher-order scheme performance in curvilinear geometries, an aspect that has received relatively less attention in the literature.

The spatial discretization algorithm consists of the subset of centered schemes that are compact (see, e.g., Refs. 6 and 8) i.e., where the spatial derivatives are computed in a coupled (implicit) fashion. As compared to explicit schemes, this approach incurs an increase in computational cost but lowers the truncation error and reduces the number of points near the boundary where special formulations are required. As a starting point, we choose the strategy developed for linear problems in Refs. 9 and 10, where a high-order finite volume approach is employed to obtain up to sixth-order schemes. However, to simplify the formal extension of higher-order accuracy to the multidimensional Navier–Stokes equations, which are nonlinear, we choose the finite difference approach (see, e.g., Ref. 11). Sections II.A and II.B outline the difference schemes employed in the formation of the various terms in the Navier–Stokes equations together with the treatment of boundary conditions (Sec. II.C).

Compact schemes have been previously employed in conjunction with explicit time-integration methods to address increasingly complex problems; see, e.g., Ref. 6. However, few such studies have focused on wall-bounded flows around geometrically complex configurations, which are of principal interest to aircraft designers. Because explicit methods are usually a poor choice for such flows—the fine mesh spacing dictates a far too stringent time-step size constraint—we select the Beam–Warming approximate factorization method[12] with the diagonalization procedure of Ref. 13 (Sec. II.D). For comparison purposes the classical fourth-order Runge–Kutta (RK) method is also implemented.

One of the principal problems encountered in the solution of the Navier–Stokes equations with centered schemes is the appearance of numerical instabilities, arising from boundary condition implementation, unresolved scales, mesh nonuniformities, and nonlinearity of the governing equations. If left unchecked, these spurious waves amplify and eventually destroy the fidelity of the solution. The impact of boundary conditions on the stability of higher-order schemes has been examined extensively, particularly for explicit time integration of model equations (see, e.g., Ref. 7). The literature reveals relatively less theoretical insight into the other complications just noted. A popular method to suppress such instabilities is through artificial dissipation in the form of a (small) additive damping term to the governing equations (e.g., Ref. 14) or through filtering. Although less popular than damping, filtering for fluid dynamics calculations is of roughly the same vintage: Ref. 15 describes an early effort. In recent years the increased use of very high-order methods has encouraged the development of correspondingly high-order filters. An extensive development of explicit filters, i.e., those not dependent on the solution of matrix systems, can be found in Refs. 16 and 17, whereas the methodology to derive implicit schemes has been outlined by Lele.[6] The filters employed in this work were derived in Ref. 10 to stabilize finite volume schemes in electromagnetic wave phenomena. The set consists of tridiagonal-based filters of up to tenth order incorporating a free parameter for control. In Sec. II.E the analysis is extended to simplify the implementation near boundaries through the optimization afforded by the free parameter.

In Sec. III a large number of canonical as well as complex problems is chosen to highlight the properties of the scheme; these range from linear two-dimensional problems on uniform meshes to the complicated flowfield past a delta wing at high angle of attack. Particular emphasis is placed on the important issues of spatial accuracy, conservation, mesh stretching, boundary condition implementation, and time integration.

II. Numerical Method

The unsteady, three-dimensional, full Navier–Stokes equations are solved in strong conservation form using general curvilinear coordinates (ξ, η, ζ):

Presented as Paper 98-0131 at the AIAA 36th Aerospace Sciences Meeting, Reno, NV, 12–15 January 1998; received 9 March 1998; revision received 18 February 1999; accepted for publication 4 March 1999.

*Technical Area Leader, Computational Sciences Branch, Aeronautical Sciences Division, Air Vehicles Directorate, AFRL/VAAC. Associate Fellow AIAA.

†Research Aerospace Engineer, Computational Sciences Branch, Aeronautical Sciences Division, Air Vehicles Directorate, AFRL/VAAC. Associate Fellow AIAA.

$$\frac{\partial}{\partial t}\left(\frac{\boldsymbol{U}}{J}\right)+\frac{\partial \hat{F}}{\partial \xi}+\frac{\partial \hat{G}}{\partial \eta}+\frac{\partial \hat{H}}{\partial \zeta}=\frac{1}{Re}\left[\frac{\partial \hat{F}_v}{\partial \xi}+\frac{\partial \hat{G}_v}{\partial \eta}+\frac{\partial \hat{H}_v}{\partial \zeta}\right] \quad (1)$$

where $\boldsymbol{U}=\{\rho, \rho u, \rho v, \rho w, \rho E\}$ is the solution vector; J is the transformation Jacobian; $\hat{F}$, $\hat{G}$, and $\hat{H}$ are the inviscid fluxes; and $\hat{F}_v$, $\hat{G}_v$, and $\hat{H}_v$ are the viscous fluxes whose details may be found in Ref. 18. The system of equations is closed using the perfect gas law, Sutherland's formula for viscosity, and the assumption of a constant Prandtl number $Pr=0.72$.

A. Treatment of Metrics and Inviscid Fluxes

The basic formula employs a five-point stencil compact difference. For any scalar quantity, ϕ in the transformed plane, which can be a metric, flux, or flow variable, the derivative ϕ' can be obtained by solving the tridiagonal system:

$$\alpha\phi'_{i-1}+\phi'_i+\alpha\phi'_{i+1}=b\frac{\phi_{i+2}-\phi_{i-2}}{4\Delta\xi}+a\frac{\phi_{i+1}-\phi_{i-1}}{2\Delta\xi} \quad (2)$$

where α, a, and b are constants that determine the spatial properties of the algorithm. The scheme is a subset of the pentadiagonal system of Ref. 6. We focus particularly on two compact schemes: the five-point, sixth-order CD6 ($\alpha=\frac{1}{3}, a=\frac{14}{9}, b=\frac{1}{9}$), and the three-point fourth-order CD4 ($\alpha=\frac{1}{4}, a=\frac{3}{2}, b=0$). Equation (2) also yields the standard explicit fourth-order E4 ($\alpha=0, a=\frac{4}{3}$, and $b=-\frac{1}{3}$) and second-order E2 ($\alpha=0, a=1, b=0$) algorithms.

Equation (2) is applied to form the various metrics $\partial x/\partial\xi$, $\partial x/\partial\eta, \ldots$, which in turn are employed to construct the Jacobian J. The inverse metrics $\partial\xi/\partial x, \partial\xi/\partial y, \ldots$ are then formed with the standard general transformation relationships. Similarly, the inviscid fluxes are first formed in transformed coordinates at each node, and each component is then differentiated with Eq. (2). The same coefficients are employed for both the metrics and the fluxes: this has been shown to limit the error on stretched meshes[10,19] (see also Sec. III.B).

B. Treatment of Viscous Fluxes

In conservative form the computation of the viscous terms in the Navier–Stokes equations is straightforward. The primitive variables u, v, w, and T are first differentiated, and the stress tensor is formed at each node. The viscous terms are then computed by another application of Eq. (2). With proper choice of sequence of operations and vectorization techniques, this successive differentiation method is efficient. However, for double-derivative terms this approach may not provide sufficient numerical stability to odd-even decoupling. Reference 6 recommends the use of second-derivative formulas with the nonconservative form of the viscous terms obtained through chain-rule differentiation. For compact schemes on curvilinear coordinates, this approach may incur a substantial computational penalty whose details depend on implementation. Between the preceding two options, an intermediate approach can be patterned after common explicit second-order implementations. This requires evaluation of certain stress-tensor quantities at midpoints of the mesh with appropriate higher-order interpolation and staggered differentiation formulas. Such schemes have been derived in Ref. 20. In the present work we have so far used the successive differentiation approach without encountering any difficulty.

C. Boundary Conditions

Boundary conditions are applied in two phases. In the first or numerical phase, boundary formulas are required to differentiate ϕ, at points 1, 2, $N-1$, and N, respectively, where the interior five-point stencil accesses points from outside the domain. In the second or physical phase, the values of the primitive variables at points 1 and N are reset based on the physical nature of the problem at these boundaries.

The formulas required for the first phase are derived after due consideration toward maintaining the tridiagonal structure of the scheme. At points 1 and 2, for example, the formulas employed are as follows.

Point 1:

$$\phi'_1+\alpha_1\phi'_2 = (1/\Delta\xi)(a_1\phi_1+b_1\phi_2+c_1\phi_3+d_1\phi_4+e_1\phi_5+f_1\phi_6+g_1\phi_7)$$

Point 2:

$$\alpha_{21}\phi'_1+\phi'_2+\alpha_{22}\phi'_3 = (1/\Delta\xi)(a_2\phi_1+b_2\phi_2+c_2\phi_3+d_2\phi_4+e_2\phi_5+f_2\phi_6+g_2\phi_7)$$

The coefficients for varying orders of accuracy can be obtained through the Taylor-series term-matching procedure. For point 1 the formulation is straightforward, and the coefficients for implicit ($\alpha_1\neq 0$) and explicit ($\alpha_1=0$) schemes may be found in Refs. 9 and 20. In this work we primarily employ fourth-order boundary conditions ($\alpha_1=3$, $a_1=-\frac{17}{6}$, $b_1=\frac{3}{2}$, $c_1=\frac{3}{2}$, $d_1=-\frac{1}{6}$, $e_1=0$, $f_1=0$, $g_1=0$). The situation is more complicated for point 2, where several options exist, depending on the desired degree of coupling of the slope at point 1 with the slopes at other points. The corresponding coefficients for various orders of accuracy, including explicit ($\alpha_{21}=\alpha_{22}=0$) and decoupled ($\alpha_{21}=0$) variants, are detailed in Ref. 20. For the cases discussed next, we choose the fourth-order $\alpha_{21}=\alpha_{22}$ option, which, for the compact cases, degenerates into the same formula as for the interior CD4 scheme.

The physical boundary conditions considered include Dirichlet (for no-slip walls) and Neumann (e.g., $\partial p/\partial n=0$, extrapolation and symmetry) types and are applied after each update of the physical variables in the interior. For the Neumann condition, high-order formulas can be easily derived.[20] The order of the chosen formulation was investigated for some of the following cases and found to have little effect on the accuracy of the solution. For physical boundaries this result may be attributable to the fact that mesh clustering is employed and local degradation in order of accuracy may be offset by the smaller mesh spacing. On the other hand the far field boundaries were sufficiently distant that boundary-condition order of accuracy was not as critical. However, some sensitivity to order of accuracy of Neumann conditions is observed at symmetry planes when mesh clustering is only modest.

D. Temporal Integration

As already noted, one of the goals of this work is to couple the compact high-order spatial discretization schemes with an implicit method. To achieve this, the Beam–Warming (BW) approximate-factorization method is chosen as implemented in the well-validated second-order flow solver designated FDL3DI (Refs. 21 and 22). For subsonic flows the scheme includes fourth-order scalar artificial dissipation.[14] This code permits execution of several built-in techniques to enhance robustness, efficiency, and accuracy, including diagonalization[13] and Newton-like subiterations. In delta form the code essentially operates under the paradigm

$$[\text{NUMERICS}]\delta U = \text{PHYSICS} \quad (3)$$

where NUMERICS denotes the original second-order three-factor implicit operator and PHYSICS constitutes the residual including the time derivative. Spatial differences in the latter can be evaluated with either the second-order, third-order upwind-biased Roe flux-difference split, or high-order compact difference schemes. The implicit time-integration method is based on either the Euler or second-order, three-point backward discretizations. To preserve time accuracy with mixed implicit/explicit spatial operators, as well as with diagonalization, Newton-like subiterations are employed. For comparison purposes the classical fourth-order Runge–Kutta (RK4) scheme has also been introduced into the code in low-storage form.[23]

E. Spatial Filtering

In Ref. 6 implicit seven-point filter formulas are presented with specific emphasis on sixth-order (pentadiagonal) and fourth-order (tridiagonal) schemes derived with Taylor series and Fourier analysis. To facilitate consistency with the interior scheme, the present work employs the tridiagonal subset developed in Ref. 10. The formulas extend to 10th-order accuracy and contain a control parameter that can be employed for optimization as described next. Denoting a typical component of the solution vector by ϕ, filtered values $\hat{\phi}$ can be obtained by solving

$$\alpha_f\hat{\phi}_{i-1} + \hat{\phi}_i + \alpha_f\hat{\phi}_{i+1} = \sum_{n=0}^{N} \frac{a_n}{2}(\phi_{i+n} + \phi_{i-n}) \qquad (4)$$

This formula provides a $2N$th-order filter with a $2N+1$ point stencil. Denoting the spectral function by SF, one can see that

$$\mathrm{SF}(w) = \frac{\sum_{n=0}^{N} a_n \cos(nw)}{1 + 2\alpha_f \cos(w)} \qquad (5)$$

where $w = 2\pi kh/L$ is the reduced wave number written in terms of the physical wave number k and the mesh spacing h. Note that, because of the symmetry of the operator, SF is real, and the filter is not dispersive. The $N+1$ unknowns $a_0, a_1, \ldots, a_N$ are derived in terms of α_f by solving the equation $\mathrm{SF}(\pi) = 0$ (eliminating the odd-even mode) and N additional equations obtained by matching Taylor-series coefficients. For example, the eighth-order filter F8 has the coefficients $a_0 = (93 + 70\alpha_f)/128$, $a_1 = (7 + 18\alpha_f)/16$, $a_2 = (-7 + 14\alpha_f)/32$, $a_3 = \frac{1}{16} - (\alpha_f/8)$, $a_4 = -\frac{1}{128} + (\alpha_f/64)$, $a_5 = 0$, whereas the second-order filter F2 has the coefficients $a_0 = \frac{1}{2} + \alpha_f$, $a_1 = \frac{1}{2} + \alpha_f$, $a_2 = a_3 = a_4 = a_5 = 0$. The α_f is retained as a free variable that must lie within the range $-0.5 < \alpha_f < 0.5$ for proper behavior of SF. The variation in SF with w at several α_f is plotted in Fig. 1a for F8. Within the preceding range of α_f, $\mathrm{SF} \leq 1$ (i.e., no wave is amplified), and, furthermore, higher values of α_f correspond to a less dissipative filter. At $\alpha_f = 0.5$ all waves are unmodified. Additional details on the specific formulas and spectral responses for various orders of accuracy may be found in Refs. 10 and 20.

The relatively large stencil of very high-order filters requires special formulations at several points near the boundaries. F8, for example, cannot be applied at points 1, 2, 3, and 4 because the stencil then extends beyond the domain. At such points one-sided high-order Padé-type formulas can be derived,[20] but SF is then complex; further, the condition that none of the waves be amplified cannot be guaranteed. An alternative technique employed in this paper is based on the observation that α_f can be considered an optimization parameter. In Fig. 1b the spectral functions for F8 and F2 are plotted for $\alpha_f = 0$ (i.e., the explicit filter) and for $\alpha_f = 0.4$. Clearly, upon reducing order of accuracy, implicit filters retain their desirable spectral characteristics far better than explicit filters. The degradation for implicit filters can be mitigated even further by increasing α_f near the boundary. The last curve in Fig. 1b indicates that the dissipation characteristics of F2 ($\alpha_f = 0.49$) approach those of F8 ($\alpha_f = 0.4$) in the resolved wave-number range $0 \leq w \leq \pi/2$, the maximum difference in SF being less than 0.4%. Thus, near the boundary, the approach followed in this work is to lower the order of accuracy of the filter coupled if necessary with a corresponding increase in local α_f. This technique is easily implemented with minimal degradation of accuracy. However, one-sided formulas can also be derived as discussed in Ref. 24.

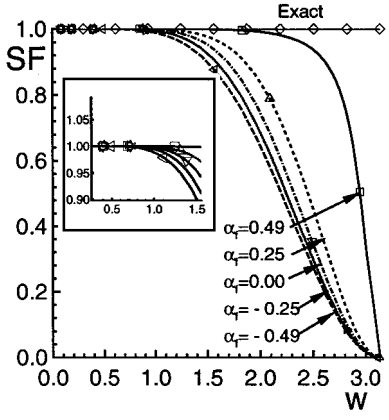

a) Response of implicit eighth-order filter for various α_f

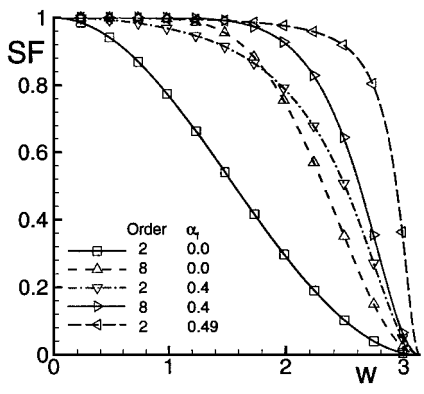

b) Effect of α_f for eighth- and second-order filters

Fig. 1 Spectral characteristics of compact filters.

Several options can be suggested for the implementation of filtering in multidimensional problems. In the following results we have followed the strategy of applying the filter to the conserved variables $\boldsymbol{U}$ after each subiteration (or after the final stage of the RK4 scheme). The filter is applied sequentially one direction at a time, and to minimize possible bias, this sequence is alternated between the various permutations. The impact of filtering on the fully discretized one-dimensional advection equation has been examined through Fourier analysis in Ref. 10. Such simplified analyses do not, however, account for boundary condition approximations, mesh nonuniformity, and nonlinearity of the governing equations, the impact of which is best assessed through actual application.

III. Results

The problems chosen to demonstrate the accuracy and robustness of the higher-order approach encompass many of the complexities encountered in fluid-dynamics calculations and constitute a collection of inviscid and viscous phenomena on Cartesian and curvilinear meshes. In the subsequent discussion the following schemes are considered: second-order with the standard scalar fourth-order damping terms (2nd), third-order MUSCL-based upwind-biased (Roe), and fourth-order (CD4) and sixth-order compact (CD6). The interior filtering formula used is denoted by appending its designation to that of the scheme. For example, CD6F10 designates the sixth-order compact scheme combined with the 10th-order filter. As noted earlier, for this study, boundary formulas for implicit spatial differencing are always CD4 while the filter order of accuracy is lowered on approaching the boundary.

A. Advection of Vortical Disturbance

The first case examined consists of the inviscid unsteady flow caused by a convecting vortex in an otherwise uniform flow with freestream Mach number $M_\infty = 0.1$. This problem compares the capabilities of the various schemes to accurately advect vortical structures as needed in direct and large-eddy simulations (DNS/LES). The initial flow condition is imposed by prescribing a vortex, centered about the location (x_c, y_c), and satisfying the following relations[25]:

$$u = U_\infty - \frac{C(y - y_c)}{R^2} \exp\frac{-r^2}{2}, \qquad v = \frac{C(x - x_c)}{R^2} \exp\frac{-r^2}{2}$$

$$p_\infty - p = \frac{\rho C^2}{2R^2} \exp(-r^2), \qquad r^2 = \frac{(x - x_c)^2 + (y - y_c)^2}{R^2}$$

where u, v, p, and R denote the Cartesian velocity components, static pressure, and vortex core radius, respectively. The nondimensional vortex strength parameter $C/(U_\infty R)$ was chosen to be 0.02. The relation for pressure was obtained by integration of $\partial p/\partial r = \rho u_\theta^2/r$ about the vortex center. The density was assumed constant, although a better approximation (using constant enthalpy) can be applied for higher vortex strengths.

The Euler equations were solved on a uniform Cartesian mesh employing four different levels of resolution ($\Delta x/R = \Delta y/R = 0.4$, 0.2, 0.1, 0.05). To examine the properties of the spatial discretization, the time-step size was reduced to $\Delta t U_\infty/R = 0.002$ [corresponding to a Courant–Friedrichs–Lewy (CFL) number of 0.04 on the finest

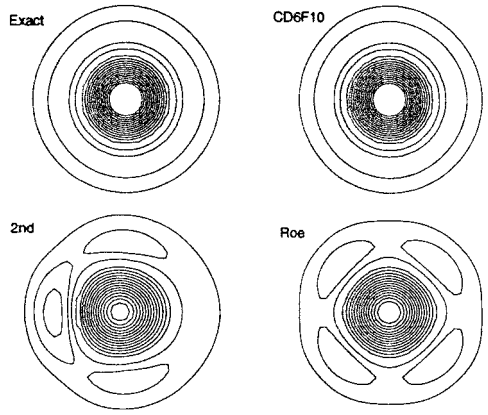

a) Vorticity magnitude contours

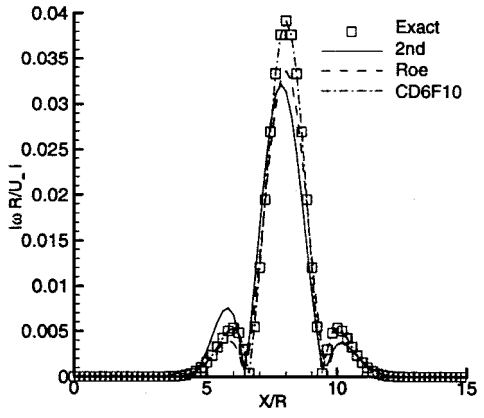

b) Vorticity magnitude along centerline

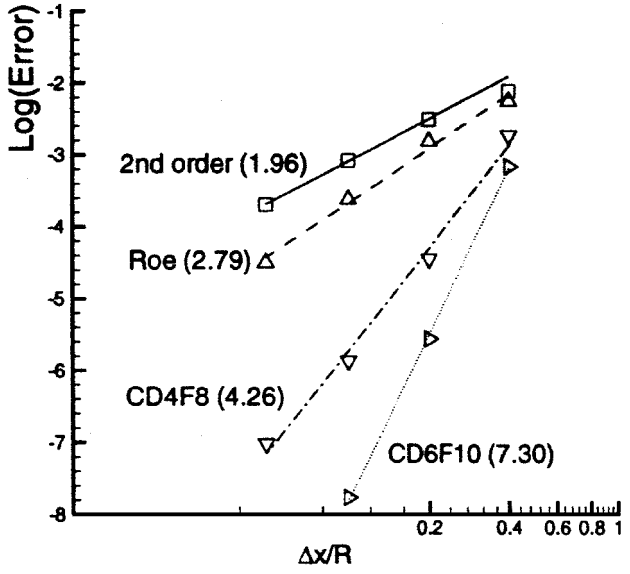

c) Order of accuracy

Fig. 2 Advection of vortical disturbance on uniform mesh with various schemes at $tU_\infty/R = 8$.

mesh] at which further reduction had no perceptible impact on solution accuracy. Additionally, for this time step size, both the BW and RK4 methods yielded identical results. Consequently only results with RK4 are discussed here.

Figure 2a shows contours of vorticity magnitude on the second grid ($\Delta x/R = \Delta y/R = 0.2$) at the instant when the vortex has convected a distance of $8R(tU_\infty/R = 8)$. A comparison of the vorticity distribution along a horizontal line passing through the vortex center is provided in Fig. 2b. Results with the compact schemes (only CD6F10 is shown) are in excellent agreement with the exact solution in terms of peak vorticity and radial symmetry. The second-order method produces significant errors in both the magnitude and radial distribution of vorticity and displays the formation of a vorticity blob, which lags the vortex. The third-order upwind-biased scheme improves the results somewhat but still exhibits significant dissipation and anisotropy errors.

A more systematic analysis of the order of accuracy and the absolute error for the various spatial discretizations is provided in Fig. 2c for second, Roe, CD4F8, and CD6F10 schemes. This figure displays the maximum error (L_∞ norm) in the computed swirl velocity along the horizontal line passing through the vortex center. In addition to the actual data points, linear least-square fits to the data (not including results on the coarsest mesh) are constructed to provide an estimate of the order of accuracy (slopes are shown in parentheses). From examination of Fig. 2c, several statements can readily be made regarding absolute error and order of accuracy. The order-of-accuracyestimates for the first three schemes are close to the expected formal accuracy values. CD6F10 is well-behaved, but the order-of-accuracy estimate is significantly higher than expected. This anomaly, displayed also by the results of Ref. 9 (albeit to a lesser degree), deserves further investigation of boundary, time-integration, and machine roundoff errors. It is anticipated that as the absolute error decreases to very low values, all of the preceding factors will exert a more dominant role in the behavior of the full discretization. For all of the grids considered the absolute error magnitude decreases consistently with the increasing formal accuracy of the algorithms. A significant reduction in the absolute error is achieved when going from the third-order upwind scheme to the compact fourth-order algorithm. For a prescribed level of accuracy (e.g., 10^{-4}), comparison of the upwind-biased and CD6F10 schemes indicates that the level of resolution (in each spatial dimension) required by the lower-order method would be more than four times that needed with the high-order scheme. Clearly, the higher-order compact algorithm could potentially result in a much smaller number of grid points for the accurate advection of three-dimensional vortical structures.

B. Advection on a Curvilinear Mesh

Although the preceding results for the high-order compact algorithm are very encouraging and informative, they have been obtained for simple uniform Cartesian meshes. To provide a more stringent and relevant assessment, the vortex-advection test case is repeated here on a smooth but highly nonorthogonal, curvilinear grid, shown in Fig. 3a. This type of mesh was constructed analytically according to the expression

$$x_{i,j} = x_{\min} + \Delta x(i-1)$$

$$y_{i,j} = y_{\min} + \Delta y_o[(j-1) + A\sin(n\pi x/L + j\phi/JL)]$$

$$\Delta x = L/(IL-1), \qquad \Delta y_o = H/(JL-1)$$

$$1 \le i \le IL, \qquad 1 \le j \le JL$$

where the amplitude, frequency, and phase-shift parameters were specified as $A = 1.0$, $n = 8$, and $\phi = 3\pi/2$. Three different levels of spatial resolution similar to the preceding test case were employed (namely, $\Delta x/R = \Delta y_o/R = 0.4, 0.2$, and 0.1). Some of the grid quality parameters for the medium mesh are maximum stretching ratio of 1.12, ratio of maximum to minimum cell size of 2.3, and maximum and mean deviation from orthogonality (skewness) of 56.4 and 40.1 deg, respectively. Therefore, it is apparent that the vortex is convected through regions of the mesh where stretching and pronounced skewness are present (Fig. 3a).

Grid-convergenceplots of the maximum error in v-velocity component are shown in Fig. 3b at a nondimensionaltime $tU_\infty/R = 8.0$. Only the central schemes are considered. The superior behavior of the high-order compact algorithm in terms of absolute error and order of accuracy is clearly manifest. It should be noted by comparison with the corresponding uniform-grid results (Fig. 2c) that order of accuracy is roughly preserved, although the absolute error increases when going to the more demanding nonorthogonal, curvilinear mesh. The second-order method displays less sensitivity to

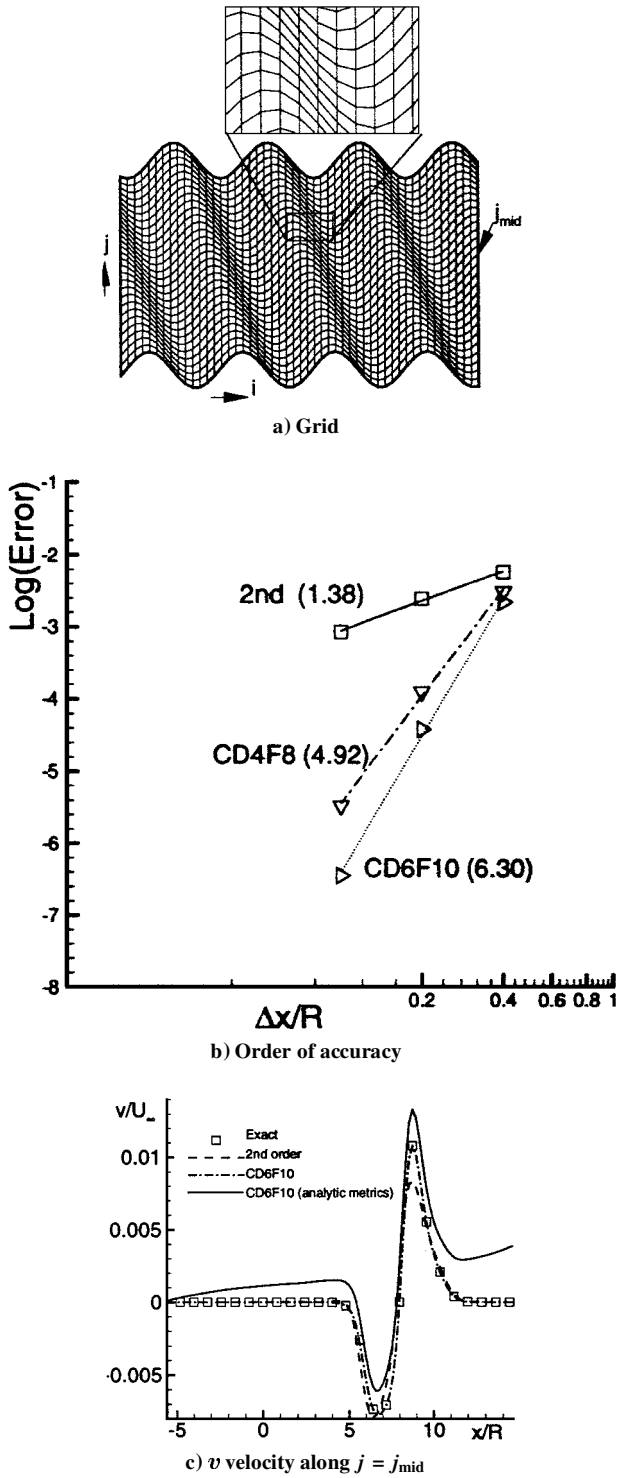

Fig. 3 Advection of vortical disturbance on curvilinear mesh with various schemes at $tU_\infty/R = 8$.

grid quality in part because the corresponding error magnitudes on the uniform mesh are much higher to start with. The superior solution obtained with the compact algorithm (CD6F10) is shown in Fig. 3c in terms of the y component of velocity along a j-constant grid line through the center of the vortex.

The curvilinear grid employed for this case provides a unique setting to investigate issues of freestream preservation noted earlier. To this effect, uniform flow was computed on the curvilinear mesh. The maximum departure from the prescribed uniform flow initial condition after one characteristic time is noted in Table 1. The second-order scheme is known to satisfy freestream preservation, and indeed all explicit centered operators possess this property in two dimensions. As seen in Table 1, metric cancellation errors with compact

Table 1 Uniform flow preservation on curvilinear mesh, $\delta u = (u - U_\infty)/U_\infty$, $\delta v = v/U_\infty$

Scheme	$\lvert\delta u_{\max}\rvert$	$\lvert\delta v_{\max}\rvert$
2nd	1.1×10^{-13}	1.1×10^{-13}
CD4F8	1.7×10^{-13}	1.4×10^{-13}
CD6F10	4.6×10^{-13}	3.2×10^{-13}

schemes are also very small. These observations do not carry over to the three-dimensional situation where special metric evaluation techniques are necessary to enforce freestream preservation.[24]

Because the present curvilinear grid is generated analytically, the convecting vortex case also was computed with analytically determined metric values. As shown in Fig. 3c for the compact sixth-order scheme, the use of the exact metric expressions results in significant errors, which are of course exaggerated on this highly distorted mesh. Improved accuracy is realized by discrete evaluation of the metrics with the same difference formula as for the other terms in the governing equations. For the one-dimensional case, this issue has been discussed in Ref. 19 for explicit and in Ref. 10 for higher-order compact schemes.

C. Evolution of Small-Amplitude Disturbance in a Shear Layer

The next case evaluates the capability of higher-order schemes to capture the temporal growth of a small-amplitude, normal-mode disturbance in an inviscid shear layer. The base parallel flow consists of a hyperbolic tangent velocity profile $u = 0.5[1 + \tanh(y)]$ and $v = 0$. (Here u, v, and y are nondimensional.) To permit comparison with incompressible theory, the freestream Mach number is set to a very small value ($M_\infty = 0.05$).

Application of inviscid linear stability theory for the evolution of small-amplitude disturbances reduces this problem to the well-known Rayleigh stability equation.[26] A detailed inviscid linear stability analysis of the hyperbolic-tangent profile has been given by Michalke.[27] Following Ref. 27, a disturbance is introduced of the form

$$\hat{u} = \frac{\epsilon \partial \Psi}{\partial y}, \qquad \hat{v} = -\frac{\epsilon \partial \Psi}{\partial x}$$

$$\Psi = Re\left[\phi(y) e^{i\alpha(x - ct)}\right], \qquad \phi(y) = \phi_r + i\phi_i, \qquad c = c_r + ic_i$$

where Ψ is the perturbation streamfunction, ϕ the eigenfunction, α the wave number, and ϵ the perturbation amplitude. The phase velocity c_r is independent of wave number and is equal to 0.5. For the present test case the most amplified disturbance is considered, which corresponds to $\alpha = 0.4446$ and $c_i = 0.2133$ (Ref. 27). The eigenfunctions $\phi_r(y)$ and $\phi_i(y)$, required to describe the initial disturbance, are computed by solving the Rayleigh stability equation with a simple relaxation procedure. The perturbation flow kinetic energy $E(t)$ is defined as

$$E(t) = \int_0^L \int_{-\infty}^{\infty} (\hat{u}^2 + \hat{v}^2)\, dy\, dx$$

where the wavelength $L = 2\pi/\alpha$ corresponds to the streamwise extent of the computational domain, on which spatially periodic conditions are applied. For small perturbation amplitudes, the temporal energy growth predicted by the linear theory is given in normalized form as $E(t)/E(0) = e^{2\alpha c_i t}$.

Calculations for the shear-layer instability were performed on three separate grids for an amplitude parameter $\epsilon = 0.001$. All cases were computed with the RK4 time-marching scheme at a nondimensional time step $\Delta t = 0.0005$. Computed results obtained with the various spatial discretizations are compared with linear stability theory in Figs. 4a–4c in terms of the normalized amplification rate. For all of the grids considered, the second-order scheme with damping is characterized by unacceptably large energy growth rates. The third-order upwind method results in significant improvement with predicted growth rates that are somewhat lower than the theoretical value, a fact attributable to the dissipative nature of the upwind

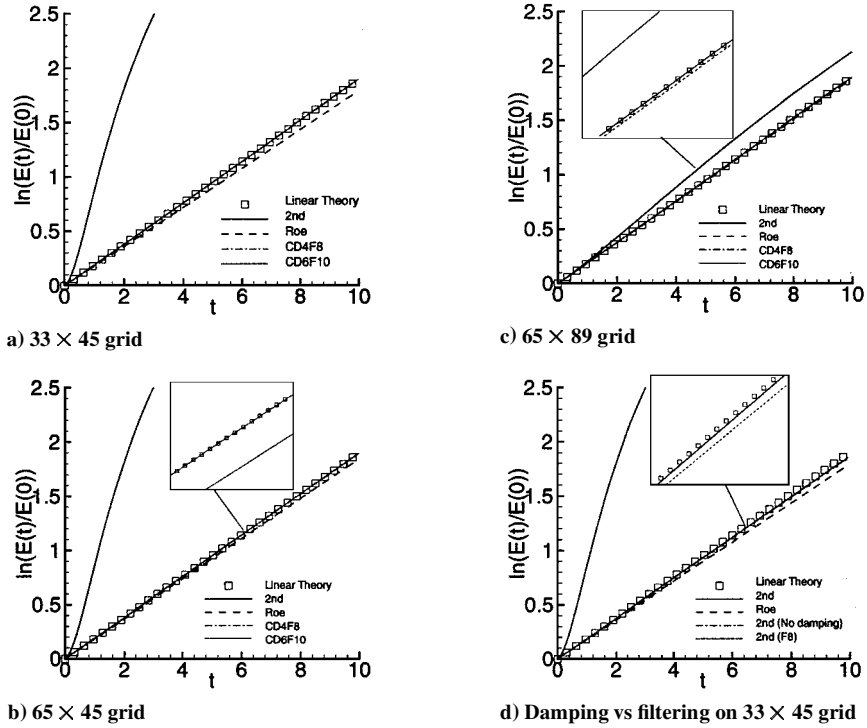

a) 33 × 45 grid

c) 65 × 89 grid

b) 65 × 45 grid

d) Damping vs filtering on 33 × 45 grid

Fig. 4 Perturbation energy growth for shear layer instability.

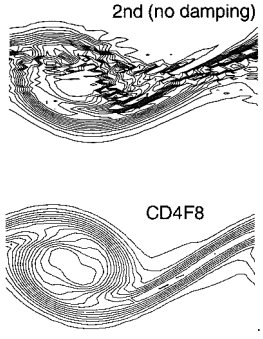

Fig. 5 Effect of high-frequency cutoff mechanism on vorticity contours in roll-up stage of shear layer instability.

algorithm. The error, however, is observed to diminish with mesh refinement, and on the finest grid the results may be considered to be satisfactory. For all of the grids employed, the superior accuracy of the compact fourth- and sixth-order schemes is evident from the predicted growth rates, which are in excellent agreement with linear stability theory. For this two-dimensional linear stability flow problem, the use of the fourth-order compact algorithm permits a reduction of grid points by more than a factor of four when compared to the upwind method.

To explore the origin of the rather poor results obtained with the second scheme, computations were performed on the coarsest mesh using the second method without damping. As shown in Fig. 4d, elimination of the fourth-order scalar damping terms significantly improves the predicted amplification rate, producing results that are actually better than those obtained with the upwind method. Similarly, the second-order scheme combined with an eighth-order filter provides much better results when compared to the standard scalar damping method. Many of the difficulties of the baseline second algorithm appear to be attributable to artificial dissipation, which introduces dramatic errors particularly for this very-low-freestream-Mach-number case. However, elimination of the damping terms without the addition of a high-frequency cutoff mechanism (such as filtering) is not a practical alternative even for this problem. Although the second-order scheme without artificial dissipation remains well behaved and stable during the initial (linear) stages of the disturbance growth, once the shear layer rolls up into a vortical structure high-frequency numerical oscillations appear: this is demonstrated in the vorticity contours of Fig. 5. The corresponding plot for the CD4F8 (Fig. 5) displays no odd–even oscillations. The high-order filter is then found to provide a robust and accurate means of suppressing the numerically induced oscillations characteristic of centered (nondissipative) schemes.

Table 2 Parameters for boundary-layer grids[a]

Grid	Dimensions	$\Delta y_{\text{wall}}/\delta$	$c_{\max}$	N_δ	$\Delta y_{\max}/\Delta y_{\text{wall}}$
$G1$	81×37	0.04	1.21	12	434
$G2$	81×61	0.02	1.13	22	556
$G3$	81×91	0.01	1.09	35	790

[a]δ = local boundary-layer thickness; c = stretching factor; N_δ = number of points in the boundary layer.

D. Flat-Plate Boundary Layer

We now proceed to problems where viscous effects are important. As a preliminary validation of the implementation of all viscous terms, the unsteady two-dimensional flow caused by the decay of a line vortex[26] was computed on a Cartesian mesh for various orientations of the line vortex. In all cases results for the high-order compact method were found to display excellent agreement with the analytic solution.

The basic problem of a steady, laminar, flat-plate boundary layer at a low freestream Mach number ($M_\infty = 0.2$) is considered next. The flow is computed on several Cartesian meshes with uniform spacing in the streamwise direction and significant stretching in the normal direction in order to provide sufficient clustering near the wall. Details of the grids employed are given in Table 2. For this relatively fine mesh spacing, characteristic of wall-bounded flows, the implicit time-integration scheme is found to be far more stable than RK4 and is employed exclusively. Furthermore, with BW, stability bounds were comparable for all spatial discretizations examined.

To illustrate the properties of the algorithms, comparison of the computed results with the Blasius solution is considered for a Reynolds number $Re_x = 1.45 \times 10^5$ based on distance from the leading edge. The computed velocity profiles on the coarse and medium meshes are shown in Figs. 6a and 6b, where $\eta = y\sqrt{(U_\infty/2\nu x)}$. Results obtained with the CD4F8 and CD6F10 schemes are in good agreement with Blasius solution, even for the coarsest grid, which

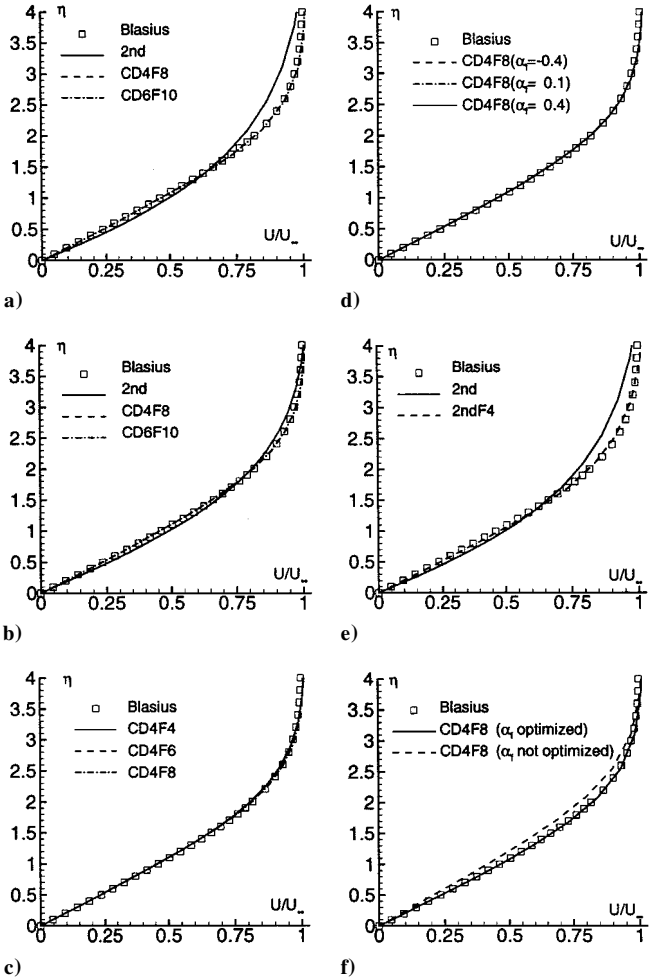

Fig. 6 Boundary-layer velocity profiles at $Re_x = 1.45 \times 10^5$. Effect of grid resolution: a) $G1$ and b) $G2$. Effect of filter on $G2$: c) order of accuracy, d) value of α_f, e) comparison of filtering vs damping, and f) effect of boundary filter optimization.

contains only 12 points within the boundary layer. The second-order scheme by contrast produces poor results for this Reynolds number on the medium grid (with more than 20 points in the boundary layer). Acceptable results (not shown) are achieved with the low-order method on $G3$, with approximately 35 points within the boundary layer. However, the error in skin-friction prediction for the second-order scheme on the finest mesh (5.2%) is still higher than the corresponding error of 1.5% displayed by the compact solutions on the coarsest grid. This result indicates that more than a factor-of-three reduction in the number of required mesh points is achieved with the compact algorithm.

The effect of the interior filter order of accuracy is assessed in Fig. 6c, which shows the computed laminar velocity profile for the CD4F4, CD4F6, and CD4F8 schemes respectively with α_f fixed at 0.4. Similarly, the effect of variation in α_f is assessed for CD4F8 in Fig. 6d with α_f values of -0.4, 0.1, and 0.4. The computed velocity profiles are observed to display practically no sensitivity to the order or coefficient of the interior filter. The maximum variation in the corresponding skin-friction coefficient is found to be less than 0.4% when α_f is varied through its recommended range ($-0.5 < \alpha_f < 0.5$).

Under conditions of relative coarse mesh density, as are likely to be encountered in complex three-dimensional calculations, details of damping/filtering techniques become important. Some of the inadequacies of the standard second scheme are again found to be associated with the fourth-order scalar artificial dissipation, which is added to maintain stability. As shown in Fig. 6e for the coarse mesh $G1$, when the second-order method is combined with a fourth-order filter (instead of damping), its accuracy improves substantially. Although not shown, conversely, the CD4 algorithm with added fourth-order damping is found to exhibit poor results, which are similar to those of the low-order scheme. These observations reassert the superior characteristics of the present fourth-order compact filter over standard scalar artificial dissipation and suggest that accuracy improvements of existing second-order codes can be achieved with a suitable filter implementation.

As noted earlier, the strategy of reducing filter order of accuracy may require proper optimization of the boundary formulation, specifically at point 2 where the order of accuracy of the filter is only second. Figure 6f shows results on $G1$ with CD4F8 with two filter coefficient setting strategies that differ only in the coefficient of α_f at point 2 (i.e., the first point away from the wall). In the optimized case α_f at point 2 is 0.499, whereas in the unoptimized case this value is 0.0, i.e., the filter is explicit. Given the poor results with the latter, clearly, the simplified strategy of lowering order of accuracy near the walls can only be justified for optimized filters. However, this is an important consideration only on rather coarse meshes: indeed note the excellent results of Figs. 6c and 6d on the medium mesh $G2$, where α_f is not modified near the wall.

E. Unsteady Flow past a Circular Cylinder

As noted in the Introduction, one of the objectives of this work is to extend the application of the high-order compact schemes to flow simulation over more practical geometries using curvilinear coordinates. Toward this end, the case of unsteady laminar flow past a circular cylinder is examined. Again, a low freestream Mach number ($M_\infty = 0.1$) is chosen to permit comparison with available incompressible computational results (e.g., Ref. 28). A baseline O-grid of size 155×201 is employed with a nonuniform spatial distribution in both coordinate directions. The far-field computational boundary is located 100 diameters away from the cylinder. A branch cut is introduced into the O-type mesh in front of the cylinder together with a five-point mesh overlap. A coarser mesh (155×101) is also constructed by removing every other radial grid line. For this wall-bounded flow the implicit BW algorithm with $\Delta t U_\infty / D = 0.005$ is employed with two subiterations.

Figure 7 exhibits the phenomenon of shedding past a cylinder at $Re_D = 1000$ computed with the second and CD6F10 schemes. The higher-order scheme is well behaved for this general configuration, which is discretized with a high-aspect-ratio, stretched, nonorthogonal mesh. Even at this low Reynolds number, results with the higher-order compact algorithm are superior: note the improved preservation of the vortex street behind the cylinder (Fig. 7).

A quantitative comparison can be made at $Re_D = 100$ with the highly resolved computations reported in Ref. 28. Table 3 displays the Strouhal number and maximum lift and drag coefficients computed with several schemes using the two grids previously described. The values for $C_{L,\max}$ and $C_{D,\max}$ obtained with the compact algorithms are observed to be in good agreement with each other as well as with the corresponding results of Ref. 28. Even on the coarser

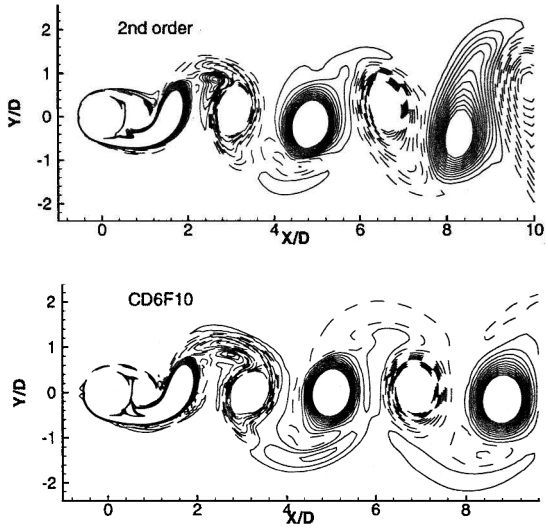

Fig. 7 Computed Kármán vortex street behind cylinder at $Re_D = 1000$.

Table 3 Strouhal number Sr and maximum lift and drag coefficients for cylinder at $Re_D = 100$

Scheme	Grid	Sr	$C_{L,\max}$	$C_{D,\max}$
2nd	155×101	0.166	0.360	1.356
2nd	155×201	0.164	0.324	1.333
CD4F8	155×101	0.162	0.316	1.302
CD4F8	155×201	0.164	0.315	1.311
CD6F10	155×101	0.162	0.316	1.306
CD6F10	155×201	0.164	0.313	1.310
Ref. 28	——	0.164	0.314	1.314

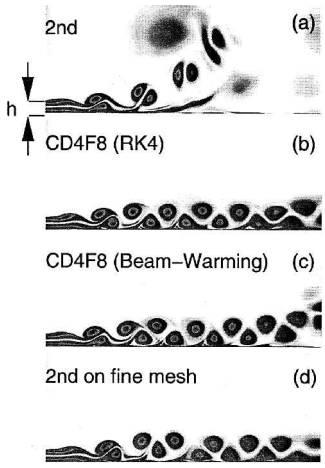

Fig. 8 Vorticity magnitude contours for two-dimensional forced wall-jet instability.

mesh, the higher-order method produces results superior to those obtained with the low-order scheme on the finer grid.

F. Forced Wall-Jet Instability

The numerical simulation of a two-dimensional transitional forced plane wall jet[29,30] presents another challenging test. The flow conditions for the simulation are selected to be as close as possible to the experiments of Ref. 29, which provide high-resolution PIV measurements. The Reynolds number is therefore fixed at $Re_h = 2150$, where h denotes the nozzle height. The jet is forced at a frequency $f = 0.15h/U_{\max}$ through a harmonic variation of the incoming parabolic velocity profile. The stretched Cartesian mesh, consisting of 230×176 points, is clustered near the plate and the nozzle exit. The highly resolved computational results of Ref. 29 are employed for scheme evaluation.

In Fig. 8 the vorticity magnitude is plotted for several methods together with the mesh-converged results of Ref. 29. The double-row vortical structure, found in the early (two-dimensional) stages of transition, is reproduced well by the present computational approach. On the coarse mesh the second-order scheme predicts spurious eruption of vortex dipoles into the freestream (Fig. 8a). In contrast, the fourth-order compact scheme with either time-integration method (Figs. 8b and 8c) provides results comparable to those obtained with the second-order algorithm on the finer mesh (Fig. 8d), which contains four times as many grid points. This has a significant impact on three-dimensional simulations, where a factor of at least eight reduction in mesh points is anticipated.

Preliminary direct numerical simulations of the three-dimensional wall-jet transition process are performed with the implicit time-integration scheme on a mesh of size $230 \times 125 \times 101$ with both the second and CD6F10 schemes. In the computations the jet is forced at the inflow plane in a manner similar to the above two-dimensional forcing function (i.e., without any spanwise modes being introduced). Figure 9 shows the computed instantaneous flow structure in terms of contours of vorticity magnitude on a plane parallel to the plate at a distance of $1.3h$. Near the nozzle exit the vortical structures arising from primary instability are fairly two-dimensional. However, in a dramatic interaction with the side walls, these primary vortices undergo a rapid breakdown caused by spanwise instabilities. This computed secondary instability process is in agreement with experimental observations as shown in Ref. 31.

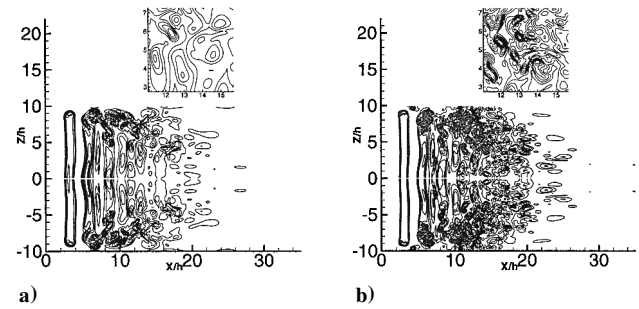

Fig. 9 Vorticity magnitude contours on $y/h = 1.3$ plane for three-dimensional wall-jet instability with a) second-order and b) CD6F10 schemes.

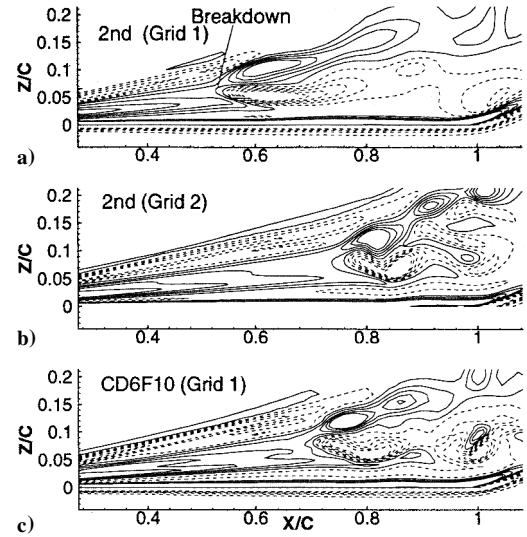

Fig. 10 Azimuthal component of vorticity on vertical plane passing through core of broken-down vortex.

From a comparison of Figs. 9a and 9b, it appears that the low-order method, although capable of capturing the primary vortical structures, fails to reproduce some of the fine-scale secondary instability structures displayed by the higher-order scheme.

G. Three-Dimensional Spiral Vortex Breakdown Above a Delta Wing

The final calculation addresses the unsteady simulation of spiral vortex breakdown above a slender delta wing with a sweep angle of 75 deg and at 32-deg angle of attack. Analysis of this complex phenomenon, which has a significant impact on aircraft control and structural integrity,[22] remains a challenge, partly because of the prohibitively large computational resources required for accurate studies. The freestream Mach number is 0.2, and the Reynolds number based on centerline chord is 9200. An extensive computational analysis with the second-order scheme, including a mesh resolution study, has been reported in Ref. 22 and will be employed for evaluation.

The delta wing is embedded in an $H - H$ topology, highly stretched mesh and represents a challenge in the implementation as well as a test of the robustness of the present scheme. Figures 10a and 10b show the instantaneous y component of vorticity on a vertical plane cutting through the vortex core for the second-order method. These results are taken from Ref. 22. Grid 2 contains double the resolution of grid 1 in the core region and was shown in Ref. 22 to be adequate. At this angle of attack, the breakdown location is highly sensitive to details of the numerical simulation. Thus, on the coarse mesh the second-order scheme results in a premature breakdown of the vortex. By contrast, the CD6F10 solution shown in Fig. 10c displays a breakdown location similar to the second-order results on the fine mesh. Focusing on the coarse mesh, the second-order method (Fig. 10a) shows relatively little detail with only two smeared concentrations of azimuthal vorticity in the vortex wake. On the other hand, CD6F10 results (Fig. 10c) exhibit a much richer structure corresponding to a stronger, tightly wound spiral in far better agreement with the grid-converged results of Fig. 10b.

H. Note on Efficiency

The preceding high-order modifications are incorporated into a fully vectorized version of the FDL3DI code for execution on a Cray C90 processor. The implementation of the compact scheme in the present implicit code does not increase memory requirements because many of the arrays necessary for flux Jacobian evaluation can be utilized for residual calculation. Because of the relatively large number of computations for the block-implicit portion, which is common to all spatial schemes, the overall cost with the CD6F10 is only about 1.9 times higher than for the second-order scheme. If diagonalization is employed, this factor increases to 2.4, which is attributable to the reduced operation count of the implicit operator. Based on the test cases just presented, we can make the conservative estimate that the number of mesh points required in each direction can be lowered by a factor of two. Consequently, in single-block mode for a three-dimensional problem, the required memory and CPU resources are reduced by factors of at least eight and four, respectively.

IV. Conclusions

Significant progress has been achieved in the extension of high-order finite difference methods for the solution of the full Navier–Stokes equations on curvilinear meshes. Fourth- and sixth-order compact spatial discretizations have been coupled with an implicit iterative time-marching approach as required for efficient solution of wall-bounded flows. The difficulties associated with high-frequency spurious oscillations—inherent to centered nondissipative discretizations—have been overcome through the application of a new high-order filter strategy. Implicit filtering operators of up to tenth-order accuracy and containing a free parameter for dissipation control have been implemented. This feature enables optimization, which in turn permits a robust and accurate treatment near boundaries.

Application to a number of increasingly complex problems, ranging from vortical advection to a full three-dimensional delta wing, confirms the superior accuracy and efficiency compared to common low-order methods. This is achieved with little reduction in the stability of the implicit time-integration operator. The order of accuracy is verified on uniform and curvilinear meshes, and freestream preservation in two dimensions is also demonstrated. For an inviscid shear-layer instability, as well as for a viscous flat-plate boundary layer with a highly stretched mesh, filtering is a superior alternative to standard scalar damping, particularly for low Mach-number flows. This suggests that the accuracy of existing codes, which employ such damping, can be improved substantially by incorporation of filtering techniques.

The preceding higher-order approach shows great promise for future DNS/LES applications for which upwind methods have been reported to be overly dissipative. Current research is focused on further analysis of time-integration effects, physical and artificial multizone boundary implementation, and the extension of the scheme to treat supersonic flows with embedded shocks.

Acknowledgments

The authors are grateful for U.S. Air Force Office of Scientific Research sponsorship under Task 2304/IW monitored by L. Sakell. This work was also supported in part by a grant of HPC time from the Department of Defense HPC Shared Resource Centers at CEWES and NAVO.

References

[1]Piomelli, U., "Large-Eddy and Direct Simulation of Turbulent Flows," *Introduction to Turbulence*, Lecture Notes, von Kármán Inst., 1997.

[2]Tam, C. K. W., and Webb, J. C., "Dispersion-Relation-Preserving Finite Difference Schemes for Computational Acoustics," *Journal of Computational Physics*, Vol. 107, No. 2, 1993, pp. 262–281.

[3]Shang, J. S., "Characteristic-Based Algorithms for Solving the Maxwell Equations in the Time Domain," *IEEE Antennas and Propagation Magazine*, Vol. 37, No. 3, 1995, p. 15.

[4]Gottlieb, D., and Orszag, S. A., *Numerical Analysis of Spectral Methods: Theory and Applications*, Vol. 26, Society for Industrial and Applied Mathematics–Conf. Board of Mathematical Sciences, Philadelphia, 1977.

[5]Canuto, C., Hussaini, M. Y., Quarteroni, A., and Zang, T. A., *Spectral Methods in Fluid Dynamics*, Springer–Verlag, New York, 1987.

[6]Lele, S. K., "Compact Finite Difference Schemes with Spectral-Like Resolution," *Journal of Computational Physics*, Vol. 103, No. 1, 1992, pp. 16–42.

[7]Carpenter, M. H., Gottlieb, D., and Abarbanel, S., "The Stability of Numerical Boundary Treatments for Compact High-Order Finite-Difference Schemes," *Journal of Computational Physics*, Vol. 108, No. 2, 1993, pp. 272–295.

[8]Hirsh, R. S., "Higher Order Accurate Difference Solutions of Fluid Mechanics Problems by a Compact Differencing Technique," *Journal of Computational Physics*, Vol. 19, No. 1, 1975, pp. 90–109.

[9]Gaitonde, D., and Shang, J. S., "Optimized Compact-Difference-Based Finite-Volume Schemes for Linear Wave Phenomena," *Journal of Computational Physics*, Vol. 138, No. 2, 1997, pp. 617–643.

[10]Gaitonde, D., Shang, J. S., and Young, J. L., "Practical Aspects of High-Order Accurate Finite-Volume Schemes for Electromagnetics," AIAA Paper 97-0363, Jan. 1997.

[11]Casper, J., Shu, C.-W., and Atkins, H., "Comparison of Two Formulations for High-Order Accurate Essentially Nonoscillatory Schemes," *AIAA Journal*, Vol. 32, No. 10, 1994, pp. 1970–1977.

[12]Warming, R. F., and Beam, R. M., "On the Construction and Application of Implicit Factored Schemes for Conservation Laws," *Symposium on CFD*, Vol. 11, Society of Industrial and Applied Mathematics–American Mathematical Society, Philadelphia, 1978.

[13]Pulliam, T. H., and Chaussee, D. S., "A Diagonal Form of an Implicit Approximate-Factorization Algorithm," *Journal of Computational Physics*, Vol. 39, No. 2, 1981, pp. 347–363.

[14]Jameson, A., Schmidt, W., and Turkel, E., "Numerical Solutions of the Euler Equations by a Finite Volume Method Using Runge–Kutta Time Stepping Schemes," AIAA Paper 81-1259, Jan. 1981.

[15]Khosla, P. K., and Rubin, S. G., "Filtering of Non-Linear Instabilities," *Journal of Engineering Mathematics*, Vol. 13, No. 2, 1979, pp. 397–433.

[16]Vichnevetsky, R., "Numerical Filtering for Partial Differential Equations," Rutgers Univ., Numerical Applications Memorandum, NAM 156, New Brunswick, NJ, Nov. 1974.

[17]Kennedy, C. A., and Carpenter, M. H., "Several New Numerical Methods for Compressible Shear-Layer Simulations," *Applied Numerical Mathematics*, Vol. 14, No. 2, 1994, pp. 397–433.

[18]Anderson, D. A., Tannehill, J. C., and Pletcher, R. H., *Computational Fluid Mechanics and Heat Transfer*, McGraw–Hill, New York, 1984, pp. 253–255.

[19]Thompson, J. F., Warsi, Z. U. A., and Mastin, C. W., *Numerical Grid Generation*, North-Holland, New York, 1985, pp. 171–179.

[20]Gaitonde, D. V., and Visbal, M. R., "High-Order Schemes for Navier–Stokes Equations: Algorithm and Implementation Into FDL3DI," U.S. Air Force Research Lab., TR AFRL-VA-WP-TR-1998-3060, Wright–Patterson AFB, OH, Aug. 1998.

[21]Visbal, M. R., "Structure of Laminar Juncture Flows," *AIAA Journal*, Vol. 29, No. 8, 1991, pp. 1273–1282.

[22]Visbal, M. R., "Computed Unsteady Structure of Spiral Vortex Breakdown on Delta Wings," AIAA Paper 96-2074, June 1996.

[23]Fyfe, D. J., "Economical Evaluation of Runge–Kutta Formulae," *Mathematics of Computation*, Vol. 20, 1966, pp. 392–398.

[24]Gaitonde, D. V., and Visbal, M. R., "Further Development of a Navier–Stokes Solution Procedure Based on Higher-Order Formulas," AIAA Paper 99-0557, Jan. 1999.

[25]Poinsot, T. J., and Lele, S. K., "Boundary Conditions for Direct Simulations of Compressible Viscous Flows," *Journal of Computational Physics*, Vol. 101, No. 1, 1992, pp. 104–129.

[26]Schlicting, H., *Boundary Layer Theory*, McGraw–Hill, New York, 1968, pp. 462–464.

[27]Michalke, A., "On the Inviscid Instability of the Hyperbolic-Tangent Velocity Profile," *Journal of Fluid Mechanics*, Vol. 19, No. 4, 1964, pp. 543–556.

[28]Kravchenko, A. G., Moin, P., and Shariff, K., "B-Spline Method amd Zonal Grids for Simulations of Complex Turbulent Flows," AIAA Paper 97-0433, Jan. 1997.

[29]Gogineni, S., Visbal, M., and Shih, C., "Experimental and Numerical Investigation of Transitional Plane-Wall Jet," AIAA Paper 97-0071, Jan. 1997.

[30]Wernz, S., and Fasel, H., "Numerical Investigation of Unsteady Phenomena in Wall Jets," AIAA Paper 96-0079, Jan. 1996.

[31]Visbal, M. R., Gaitonde, D. V., and Gogineni, S. P., "Direct Numerical Simulation of a Forced Transitional Plane Wall Jet," AIAA Paper 98-2643, June 1998.

J. Kallinderis
Associate Editor